MRI-Powered Robotics

Aaron T. Becker, Ouajdi Felfoul, Li Huang and Pierre E. Dupont

Abstract Magnetic Resonance (MR) scanners provide high-resolution imaging of soft tissue. An unexploited capability of these systems is that they can also wirelessly power, track, and control robots placed inside their bore. Such robots can be fabricated from inexpensive materials and their control can be accomplished entirely through scanner programming. This technology may enable new MR-guided interventions as well as facilitate current procedures. This paper reviews recent developments in MRI-powered robots, and investigates three case studies: (1) high-speed control of an actuator rotor, (2) independent, simultaneous control of n rotors, and (3) MRI-based navigation and propulsion of millirobots that self-assemble into a tool for penetrating tissue. These approaches are illustrated through analytical modeling and experiments in a clinical MRI scanner.

1 Introduction

Robotics offers important contributions to image-guided, minimally invasive surgery. MRI has several advantages over other imaging techniques. MRI does not use ionizing radiation, yet provides high resolution soft-tissue imaging. Examples of image-guided, minimally invasive surgery include an MR-powered swimming endoscope [1] and an intravascular swimming robot [2, 3, 4]. In [1], a sinusoidal electric current through a series of wire coils on a tail induced a magnetic field that interacted

Aaron T. Becker and Li Huang
Department of Electrical and Computer Engineering, University of Houston, Houston, TX 70004, USA, e-mail: atbecker@uh.edu, e-mail: lhuang21@uh.edu

Ouajdi Felfoul and Pierre E. Dupont
Department of Cardiovascular Surgery, Boston Children's Hospital and Harvard Medical School, Boston, MA, 02115 USA e-mail: firstname.lastname@childrens.harvard.edu.
This work was supported by the National Science Foundation under Grant IIS-1208509, the Wyss Institute for Biologically Inspired Engineering, and the University of Houston ECE Department.

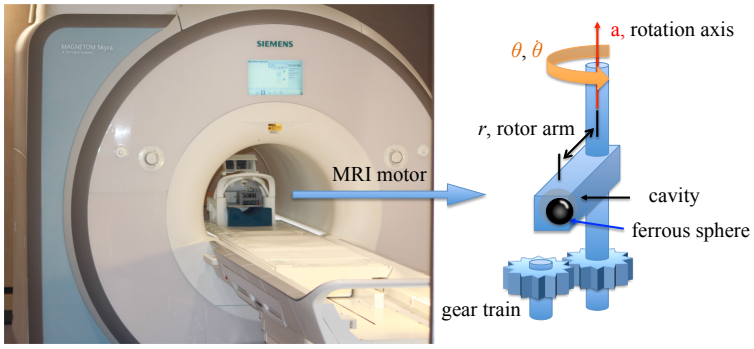

Fig. 1 An MRI-powered motor inside a clinical scanner. Control of motor position and torque is enabled by interleaved imaging and actuating pulse sequences. These track motor angle and generate appropriate magnetic-gradient-based forces.

with the static field of the MR scanner to undulate the tail. Alternatively, in [2, 3, 4] magnetic gradients, normally used for MR-signal spatial encoding, were exploited to propel an intravascular robot by inducing forces on ferromagnetic material.

MR image-guided procedures, however, pose several challenges for robotics [5, 6, 7, 8, 9]. First, the magnetic fields used in an MRI produce forces on all ferrous materials in the robot, turning these materials into strong magnetic dipoles that apply torque to align with the MRI's static field and exert forces on each other. Second, ferrous materials create imaging artifacts and must be isolated from the imaging region of interest. Third, MRI gradients induce currents in conducting materials, which can generate dangerous amounts of heat and create viscous damping forces.

Despite these challenges, there are several recent innovations demonstrating inexpensive, tetherless actuation powered, imaged, and controlled using MRI. Martel et al. controlled in vivo a mm-scale particle in a swine carotid artery [7]. Vartholomeos et al. designed an MRI-powered single-DOF actuator to build a tetherless biopsy robot [8]. This was extended to closed-loop control of a single actuator in [9].

Centimeter-scale MRI-powered and imaged robots are small enough to fit inside the MRI bore, enabling access of hard-to-reach mid-torso locations. While a variety of MR-compatible robots for surgical procedures ranging from heart surgery to brachytherapy and needle-biopsy have been developed [10, 11, 12, 13, 14, 15, 16], all require high-cost actuators and require either electrical or mechanical tethering to external control systems.

In contrast, MRI-powered actuators, as shown in Fig. 1, can be fabricated inexpensively from plastic parts and metal spheres. MRI-based robotic technology could be rapidly and inexpensively disseminated because it requires only scanner software and inexpensive actuator components, the majority of which can be 3D printed [17]. They require no tethers because they can be imaged, powered, and controlled directly by the MRI scanner [8, 9, 18].

This approach can be explained by analogy with an electric motor. The MR scanner is the stator and the rotor is composed of an axle attached to a lever arm with a cavity containing a ferrous sphere. Rotating MRI gradients generate forces on this ferrous sphere, which causes rotor motion. Because the sphere is in a cavity, it can remain aligned with the scanner's $\mathbf{B}_0$ field during rotor rotation.

While [7, 8, 9, 18] demonstrated control of a single particle or a single rotor, many clinical applications require multiple DOF. This is challenging because the three orthogonal magnetic gradients of an MRI are applied over the entire scanner bore, often making the resulting control problem underactuated. Demonstrating controllability and deriving control laws requires techniques from nonlinear control theory.

Finally, millimeter-scale magnetized robots could navigate through the natural fluid-filled passageways of the body, including the circulatory system and cerebrospinal fluid spaces. Navigating through these passages could enable highly localized therapies with minimal trauma. However, it is often necessary to penetrate into the tissue surrounding these passages. Examples include delivering a drug to a tissue location several centimeters from a fluid-filled space, puncturing a membrane to release trapped fluid, or opening a blocked passageway. Tissue penetration is difficult because it requires substantially higher forces than those needed to propel a millirobot through a bodily fluid. Prior tetherless systems for moving through tissue require large external magnets to either rotate threaded magnetic cylinders through muscle tissue [19] or pull magnetic spheres through brain tissue [20].

The contribution of this paper is to review recent advances in the design and methodology for robots actuated, imaged, and controlled by MRI. Section 2 provides basic theory on how MRIs can apply forces to and track ferrous particles. This is followed by three case studies: Section 3 on how an MRI can power, image, and control a single motor and describes an actuator that produced over 9N of force, Section 4 on controlling multiple MRI-motors simultaneously, and Section 5 on storing magnetic energy and releasing this energy for tissue penetration using self-assembling robots steered by MRI. Section 6 ends with suggestions for future research directions.

2 Theory

Powering, tracking, and controlling MRI-guided robots requires three components: applying magnetic forces, measuring robot position, and designing pulse sequences for control.

2.1 Magnetic Forces in an MR Scanner

Magnetization: a ferrous particle in the strong static field of an MRI scanner becomes a magnetic dipole. Its magnetization magnitude per unit volume of the material asymptotically approaches the saturation magnetization $\mathbf{M}_s = [M_{sx}, M_{sy}, M_{sz}]^\intercal$. The MRI gradient coils produce the magnetic field $\mathbf{B}_g(t)$. The force exerted on the ferrous particle by $\mathbf{B}_g(t)$ is

$$\mathbf{F}(t) = v\,(\mathbf{M}_s \cdot \nabla)\,\mathbf{B}_g(t) = vM_{sz}\left[\frac{\partial B_{gz}}{\partial x}, \frac{\partial B_{gz}}{\partial y}, \frac{\partial B_{gz}}{\partial z}\right]^\intercal(t). \tag{1}$$

Here v is the volume of the ferrous material. The magnetic field $\mathbf{B}_g(t)$ corresponds to the three orthogonal gradient coils and is designed to produce three independent gradients: it has been reasonably assumed that $M_{sz} \gg M_{sx}, M_{sy}$. These three gradients apply three independent forces on any ferromagnetic object inside the MRI, as shown in Fig. 2.

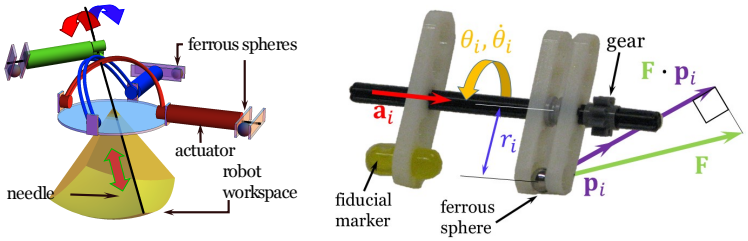

Fig. 2 (left) Three independent rotors arranged as actuators for a biopsy robot, inspired by [21]. (right) MRI-powered, single-DOF rotor with gear for power transmission.

Dipole interaction: magnetized ferrous particles exert forces on each other. Dipole forces overpower MRI gradient forces when the dipoles are closer than a threshold distance. A spherical magnet at position $\mathbf{p}_1$ with magnetization $\mathbf{m}_1$ generates the following magnetic field at position $\mathbf{p}_2$ [22]:

$$\mathbf{B}_{\mathbf{p}_1}(\mathbf{M}_{\mathbf{p}_1}, \mathbf{p}_2) = \frac{\mu_0}{4\pi}\frac{3\mathbf{n}_{12}(\mathbf{n}_{12} \cdot \mathbf{M}_{\mathbf{p}_1}) - \mathbf{M}_{\mathbf{p}_1}}{|\mathbf{p}_2 - \mathbf{p}_1|^3}, \tag{2}$$

with $\mathbf{n}_{12} = (\mathbf{p}_2 - \mathbf{p}_1)/|\mathbf{p}_2 - \mathbf{p}_1|$. This is the *magnetic field of a dipole*. The force applied to a dipole at $\mathbf{p}_1$ with magnetic moment $\mathbf{M}_{\mathbf{p}_1}$ by another dipole at $\mathbf{p}_2$ with magnetic moment $\mathbf{M}_{\mathbf{p}_2}$ is approximated by

$$\begin{aligned}\mathbf{F}_{12} \approx \frac{3\mu_0}{4\pi}\frac{1}{|\mathbf{p}_2 - \mathbf{p}_1|^4}\Big[5\mathbf{n}_{12}\Big((\mathbf{M}_{\mathbf{p}_1} \cdot \mathbf{n}_{12})(\mathbf{M}_{\mathbf{p}_2} \cdot \mathbf{n}_{12})\Big) \\ -\mathbf{n}_{12}(\mathbf{M}_{\mathbf{p}_2} \cdot \mathbf{M}_{\mathbf{p}_1}) - \mathbf{M}_{\mathbf{p}_1}(\mathbf{M}_{\mathbf{p}_2} \cdot \mathbf{n}_{12}) - \mathbf{M}_{\mathbf{p}_2}(\mathbf{M}_{\mathbf{p}_1} \cdot \mathbf{n}_{12})\Big].\end{aligned} \tag{3}$$

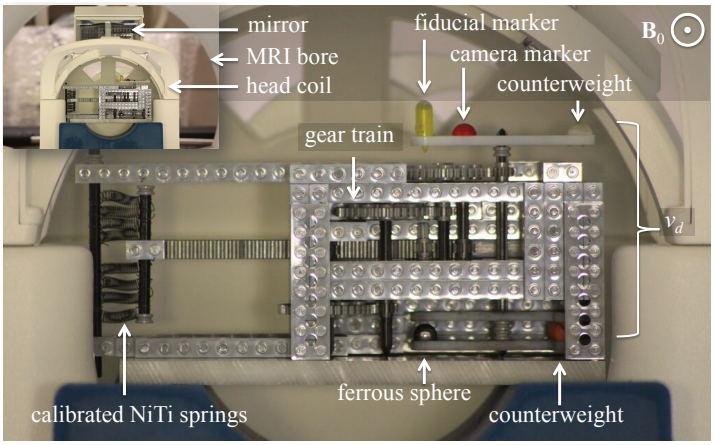

Fig. 3 The prototype actuator used for single-rotor experiments, pictured inside the MRI scanner.

2.2 Fast Fiducial Imaging

A ferrous particle in fluid can be tracked by detecting the signal void. The motor shown in Fig. 3 operates in air, and requires a different tracking method that uses RF-selective excitation to detect a passive fiducial marker.

RF-selective excitation uses the magnetic field of the ferrous particle as a slice-selection gradient. Rotor tracking requires attaching the fiducial marker to the rotor at some position where it remains in the excited region for all possible rotation angles. This excited region is determined by the RF frequency and bandwidth, but is always aligned with the $\mathbf{B}_0$ field. The region is torus-shape for RF frequencies less than the Larmor frequency or two tear-drop shapes extending from the particle above the Larmor frequency, as shown in Fig. 4. If all tissue lies outside the excited region, an image using RF-selective excitation will show only the marker because the actuator does not contain hydrogen atoms and is invisible. Simple image processing can then determine rotor angle.

To image a fiducial marker positioned at $\mathbf{p_m}$, the central frequency of the RF pulse is a function of $\mathbf{B_p}$:

$$f = \frac{\gamma}{2\pi}\left[\mathbf{B_p}(\mathbf{M_p}, \mathbf{p}_m) + \mathbf{B}_0\right]\hat{z} \tag{4}$$

where γ $[\frac{\text{rad}\times\text{Hz}}{\text{T}}]$ is the gyromagnetic ratio of hydrogen, $\mathbf{B}_0$ is the homogeneous MRI field, and $\hat{z}$ is the unit vector along the MRI bore axis.

Additionally, the RF pulse should avoid tissue excitation by not containing the Larmor frequency corresponding to $\mathbf{B}_0$:

$$f - \frac{\text{BW}}{2} > \frac{\gamma}{2\pi}\mathbf{B}_0\hat{z}, \qquad \text{or} \qquad f + \frac{\text{BW}}{2} < \frac{\gamma}{2\pi}\mathbf{B}_0\hat{z} \tag{5}$$

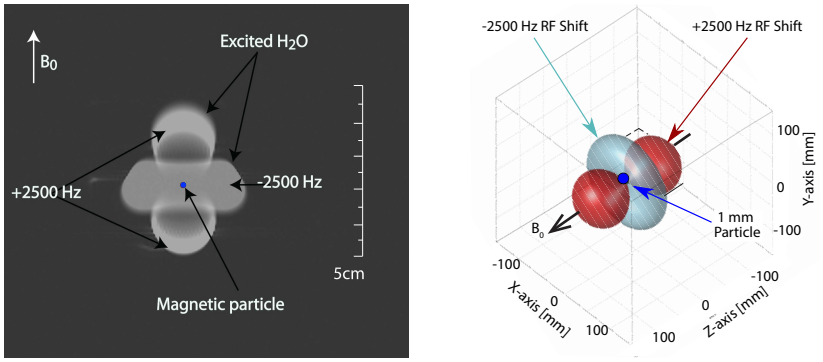

(a) superimposed MRI images (b) simulation of excited region

Fig. 4 RF-selective excitation of a 1mm radius magnetic particle. RF pulses shifted below and above the Larmor frequency generate different excited regions aligned with the $\mathbf{B}_0$ field.

2.3 Closed-Loop Pulse Sequence Design

The MRI scanner must interleave sensing and actuation to control the rotor. Many applications could be served by a multi-loop controller. An inner loop, performing rotor control as described in this section, would operate at a high frequency while an outer loop, performing standard tissue imaging, would operate at a lower rate.

Most commercial MR imaging sequences do not operate in real time. To achieve real-time tracking, the proposed technique uses single-dimensional pulse sequences, as in [2, 8, 9, 23, 24]. These sequences have short gradient durations and do not generate unwanted rotor motion. They are termed "single-dimensional" because they provide an aggregate signal in one dimension. Because the particle's magnetic gradient excites the fiducial marker, no slice-select gradient is required.

3 Case Study A: Commutation Control of a Single Rotor

An MRI scanner can apply controllable forces—but not torques—to ferrous materials. However, placing a ferrous particle on a lever arm connected to an axle creates a *rotor* for applying torque. To maximize torque, magnetic forces should be directed perpendicular to the rotor. This is called *commutation control*, and was explored in [18].

Since this approach differs fundamentally from traditional MRI programming, its development required engineering innovations. First, RF-selective signatures were used to track fiducial markers. Second, Kalman filtering improved the estimation of the angular position and velocity of a moving rotor. Third, closed-loop commutation control was exploited to interleave imaging and actuation pulse sequences. These innovations on a clinical MRI scanner enabled maximization of motor torque and velocity, avoidance of slip, and regulation of motor angle.

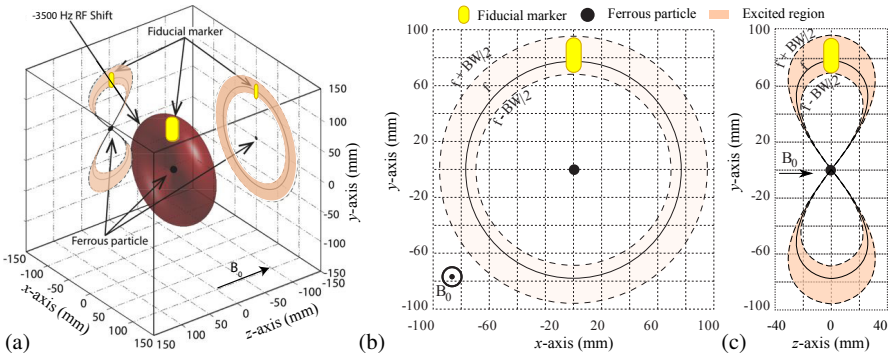

Fig. 5 Region of RF-selected excitation. (a) 3D view with projections, (b) XY plane, (c) ZY plane. Solid lines indicate surface excited at central RF frequency; dashed lines indicate volume excited over bandwidth.

A series of experiments were performed to evaluate closed-loop commutation control. All experiments used the prototype actuator shown in Fig. 3. Real-time communication was achieved using the Siemens Integrated Development Environment for Applications (IDEA). A Canon single-lens reflex video camera (model T1i) was used to record rotor position for ground truth measurements by mounting an angled mirror behind the prototype, and placing the camera on a tripod outside the 5-Gauss line.

3.1 Optimizing Fiducial Location and Imaging Parameters

Section 2.1 explained that a fiducial marker is necessary for rotor tracking. All experiments used a capsule-shaped MR-SPOT (Beekley Medical, CT) fiducial marker, whose location was optimized for imaging the ferrous particle contained within the actuator. The required RF-pulse bandwidth with respect to the vertical distance v_d is shown in Fig. 5. The dashed lines correspond to the bandwidth of a 1 ms RF pulse (2.5 kHz), the nominal pulse width. For this pulse width the optimal vertical offset to excite the full marker volume without causing background excitation is $85 \leq \mathrm{v}_d \leq 94$ mm.

These selections of r_d and v_d define $\mathbf{P}_m(r_d, \mathrm{v}_d)$, (2), and (4) were used to solve for an RF-offset of -3.5 kHz. Given the choice of BW $= 2.5$ kHz in the paragraph above, it can be verified that these values satisfy (5) ensuring that no signal emission from tissue will arise during fiducial tracking. The resulting volume of excitation around the ferrous sphere is depicted in Fig. 5a. The fiducial marker is entirely within the excited region and its excitation is independent of rotor angle.

3.2 State Estimation

Imaging was performed using a 32-channel head coil. However, as the rotor moves, the signal detected by each channel varies. A weighted average $\bar{S}$ was used:

$$\bar{S} = \sqrt{\sum_{i=1}^{32} cnr_i S_i^2}, \qquad cnr_i = \frac{CNR_i}{\sum_{j=1}^{32} CNR_j}, \qquad CNR_i = \frac{|S_A - S_B|}{\sigma_{\circ B}}. \tag{6}$$

Here S_i is the signal detected by the i^{th} channel and cnr_i is the *Contrast-to-Noise Ratio* of the i^{th} channel, where S_A is the maximum value measured in the region containing possible marker positions, while S_B and $\sigma_{\circ B}$ are the maximum value and standard deviation measured outside that region. Higher CNR values correspond to higher peak detection accuracy. CNR was used to assess the effects on tracking due to nearby tissue, sampling rate, and rotor velocity.

The rotor position can be measured several times per second, but the control law input to the MRI requires the position and velocity several hundred times per second. To provide state estimates between measurements as well as to compensate for imaging noise, Kalman filtering is employed. The state equations at step k are linearized about the estimated state given all sensor measurements at time k. Following the standard approach, estimation is split into *predicting* the current state using previous measurements and the process model, and *correcting* the estimate using MRI measurements.

3.3 Maximum Torque Control

Closed-loop commutation was used to measure the maximum output torque. The overall pulse sequence includes a variable length actuation sequence. Increasing the length of this actuation sequence increases the relative amount of time spent actuating versus imaging the rotor. This decreases the rotor angle measurement rate, however, resulting in a less accurate estimate of rotor angle. To investigate this tradeoff, experiments were performed for a set of 11 actuation durations, t_{act}. Results are reported in terms of duty cycle, $\frac{t_{\text{act}}}{t_{\text{act}}+t_{\text{off}}}$, where t_{off} is defined as imaging time + 0.5ms to account for the ramp up and ramp down time of the actuation gradient.

To provide a comparison with prior work, open-loop commutation experiments were also performed with a sinusoidal gradient force of frequency ω. Starting from arbitrary initial conditions, the rotor eventually synchronizes with the applied gradient force.

Three trials were run for each controller configuration. Representative trials of closed- and open-loop commutation are presented in Fig. 6. The depicted closed-loop trials correspond to $t_{\text{act}} = \{40, 50, 80, 120, 225\}$ ms while the open-loop trials are for $\omega/2\pi = \{0.25, 0.5, 1, 1.5, 1.75\}$ Hz. With closed-loop control, the actuator rotates at high velocity ($\sim$10Hz) that gradually decreases with an increasing load

until the stall force is reached. In contrast, open-loop commutation results in lower forces attained over significantly longer time periods.

Furthermore, in open loop, the rotor eventually slips, i.e., falls out of synchrony with the rotating gradient force. Rotor slipping was never observed in closed loop. Closed-loop control attains higher maximum forces and is up to twice as fast as the best open-loop control. In closed-loop control, the maximum force occured for $t_{\text{act}} = 120\,\text{ms}$ corresponding to an 84.6% duty cycle.

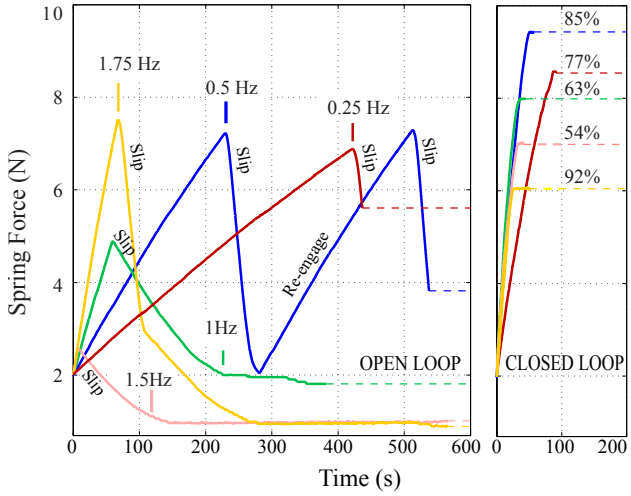

Fig. 6 Spring force versus time for MRI actuation starting at t=0. (a) Open-loop commutation. Labels indicate input frequency. (b) Closed-loop commutation. Labels express actuation duty cycle as a percentage. Dashed lines in (a) and (b) indicate steady-state spring extension.

4 Case Study B: Multi-Rotor Control

Case Study A demonstrated tracking and controlling of a single rotor capable of actuating a single degree of freedom (DOF). However, many clinical applications require multiple DOF. This is challenging because the three orthogonal magnetic gradients of an MRI scanner are applied over the entire scanner bore, so with large numbers of rotors the resulting control problem is underactuated. For such underactuated systems, inhomogeneity of subsystems can be exploited to achieve controllability. This has been considered in the context of independently controlling the motion of multiple millimeter-scale robots [25, 26, 27] and also for the case of simultaneously controlling n rotors [28].

This section models rotors that constrain the ith ferrous sphere to rotate about an axis $\mathbf{a}_i$ with a moment arm of length r_i. Each rotor's configuration is fully described

by its angular position and velocity $[\theta_i, \dot{\theta}_i]^\intercal$, as shown in Fig. 2. The configuration space of all n rotors is $\mathbb{R}^{2\times n}$.

A closed-loop controller can be designed using a control-Lyapunov function [29] to enable robust, multi-axis control. The multi-rotor velocity control problem is to find inputs such that for any $\boldsymbol{\theta}(0)$ and desired angular velocities $\boldsymbol{\omega}$,

$$\lim_{t\to\infty} \sum_{i=1}^{n} \left\| \dot{\theta}_i(t) - \omega_i \right\|_2 = 0. \tag{7}$$

For ease of analysis, the simplified rotor dynamics $\ddot{\theta}_i(t) = \frac{r_i}{J_i}\mathbf{F}(t)\cdot\mathbf{p}_i(t)$ will be used. A control law must select the three magnetic gradients $\mathbf{F}(t)$ that decrease (7), and so a suitable Lyapunov function candidate is the sum squared velocity error:

$$V(\boldsymbol{\theta},\dot{\boldsymbol{\theta}},t) = \frac{1}{2}\sum_{i=1}^{n}\left(\omega_i - \dot{\theta}_i(t)\right)^2, \qquad \dot{V}(\boldsymbol{\theta},\dot{\boldsymbol{\theta}},t) = \sum_{i=1}^{n}\left(\omega_i - \dot{\theta}_i(t)\right)\ddot{\theta}_i(t) \tag{8}$$

$$= \mathbf{F}(t)\cdot\sum_{i=1}^{n}\left(\omega_i - \dot{\theta}_i(t)\right)\frac{r_i}{J_i}\mathbf{p}_i(t)$$

Control inputs were designed to make $\dot{V}(\boldsymbol{\theta},\dot{\boldsymbol{\theta}},t)$ negative semi-definite:

$$\mathbf{f} = \operatorname{sgn}\left(-\sum_{i=1}^{n}\left(\omega_i - \dot{\theta}_i(t)\right)\frac{r_i}{J_i}\mathbf{p}_i(t)\right)$$

$$\mathbf{F}(t) = g_M v_i M_{sz}\begin{cases}[1,1,1]^\intercal & \text{if } \mathbf{f}\equiv 0 \text{ and } \dot{\boldsymbol{\theta}} \neq \boldsymbol{\omega} \\ \mathbf{f} & \text{else}\end{cases} \tag{9}$$

A *signum function* $\operatorname{sgn}(\cdot)$ is -1 for a negative input, 0 for the input zero, and +1 for a positive input. The $\operatorname{sgn}(\cdot)$ ensures that the desired velocity $\dot{\boldsymbol{\theta}} = \boldsymbol{\omega}$ is the only invariant state. There are other configurations where $\dot{V}(\boldsymbol{\theta},\dot{\boldsymbol{\theta}},t) = 0$, but in such cases the control law (9) generates a nonzero acceleration $\ddot{\theta}_i(t)$—without increasing $V(\boldsymbol{\theta},\dot{\boldsymbol{\theta}},t)$—therefore some rotors will change velocities. This ensures that the system has global asymptotic stability.

Position control is made possible by implementing a PID feedback loop around (9). Fig. 7 shows simultaneous convergence to angular positions for 5 and 25 rotors. Convergence time increases with the number of rotors. With no load there is asymptotic convergence to the goal position, but a non-zero load oscillates about $\boldsymbol{\theta}_{\text{goal}}$ because most final configurations cannot be statically held by a constant gradient field. These MATLAB simulations are available online [28].

Localizing several rotors with line scans is difficult because their projections can overlap. Each marker must be disjoint in two non-parallel projections that are also not parallel with the marker's axis of rotation. Ideally, the rotors and their projections are arranged so the paths of the markers do not intersect in any projection. In this way, n rotors can be simultaneously tracked by two line scans, followed by detecting n non-intersecting peaks on each projection. This approach is illustrated in Figs. 8

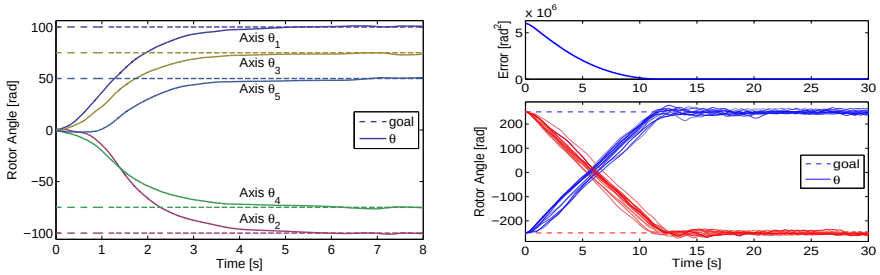

(a) 5 rotor control, positions under load (b) 25 rotor control, positions under load

Fig. 7 Simulated position control of multiple non-parallel rotors using control law (9).

and 9, showing two orthogonal projections for tracking three rotors. This tracking sequence requires 18ms, enabling real-time positioning of the rotors.

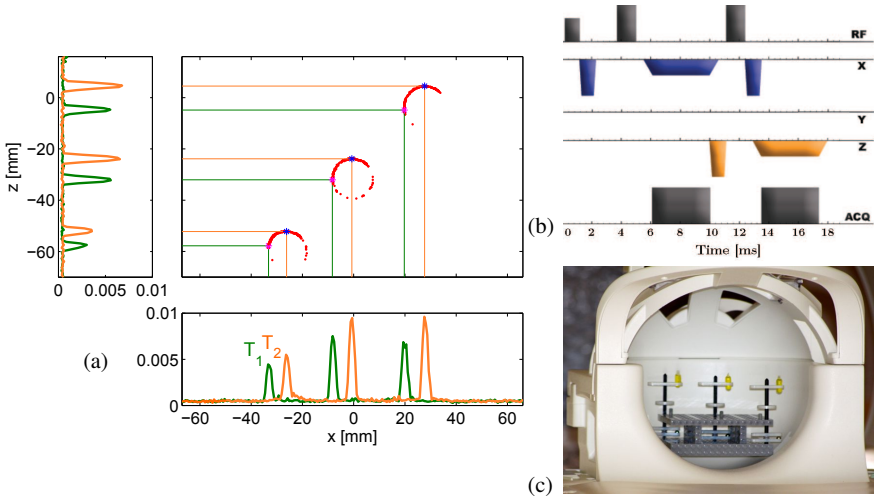

Fig. 8 (a) Simultaneous tracking of three rotors with two line scans. (b) Pulse sequence design for tracking rotors. (c) Three rotors in an MRI head coil.

To analyze the preceding topics in the context of a practical example system, a three-axis biopsy robot was designed, inspired by a model using DC motors [21]. Figure 2 shows a schematic of the proposed system. The robot has a base for mounting on the patient. Two actuators control orthogonal axes of a nested spherical yoke and a third actuator drives the needle.

Fast real-time control requires fast tracking. Rotors must be arranged to minimize the number of line scans required to localize the markers. The design shown in Fig. 9 can detect the position of each rotor with just two line scans. The line scans along

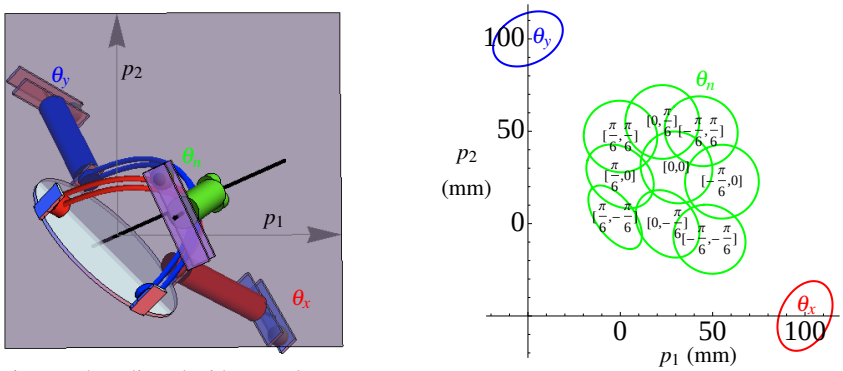

Biopsy robot aligned with scan plane θ_i projections onto scan plane

Fig. 9 Needle biopsy robot, designed so two orthogonal line scans can localize all three rotors. The ellipses parameterized by θ_i are disjoint for all configurations of $[\theta_x, \theta_y] \in [-\pi/6, \pi/6]$.

p_1=[-1,2,2] and p_2=[2,-1,2] are orthogonal. The projections for the three rotors are disjoint in both p_1 and p_2, and all values of $[\theta_x, \theta_y] \in [-\pi/6, \pi/6]$ result in ellipses.

5 Case Study C: an MRI Gauss Gun

While millimeter-scale MRI-powered robots have been proposed to deliver therapeutics by swimming through the fluid-filled passages of the body, the maximum forces that can be produced by clinical gradient coils are relatively weak—approximately 40% the force of gravity. While these forces can enable robot navigation, they are insufficient to produce tissue penetration, which may be necessary for effective delivery of the therapy. Tissue puncture force, however, is inversely related to penetration velocity [30]. This motivates using energy storage and sudden release to perform penetration.

The magnetic attraction forces between particles inside the scanner are much larger than the gradient forces that the scanner can apply. The approach here exploits this fact by storing magnetic energy in individual millirobots. These millirobots are individually navigated to a target location. At the target location the millirobots self-assemble, and in the process convert the stored potential energy into kinetic energy for tissue penetration [31].

The design was inspired by a children's toy called a *Gauss gun*. In a toy Gauss gun magnetic potential energy is stored by a particular arrangement of permanent magnets and steel spheres. Introducing a sphere to the trigger side of the arrangement releases this potential energy in a sudden and dramatic chain reaction, and fires a sphere from the opposite side. The exit velocity is many times faster than the entry velocity, and can be increased by adding additional stages and/or larger magnets.

The MRI Gauss gun does not need permanent magnets because steel is highly magnetized by the 3T magnetic field of an MRI. It consists of a *trigger*, one or more *barrels*, and an optional *delivery* component. Each barrel contains two magnetized

spheres separated by a nonmagnetic spacer. This arrangement is individually stable. Using existing control approaches [25, 26], barrels can be navigated through fluid-filled spaces and self-assembled at a desired penetration location. The assembly can then be fired by attaching a special trigger module. The trigger consists of two spheres separated by a spacer longer than that used in the barrels. After firing, the forces joining the components are reduced and the Gauss-gun can be disassembled and navigated out of the body.

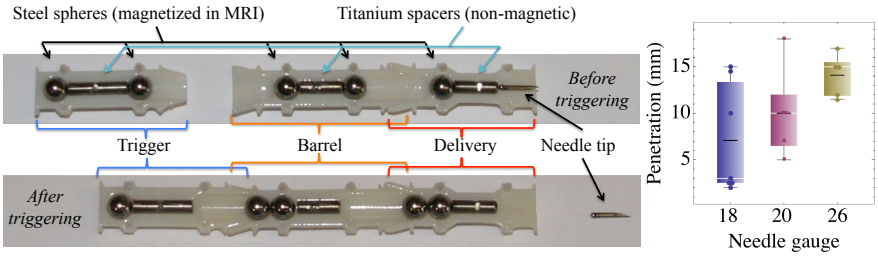

Fig. 10 (Left) cut-away images of Gauss gun components. A *trigger* fires the Gauss gun. Multiple *barrel* components can be stacked to achieve stronger forces. An optional *delivery* can be used to administer the desired treatment. (Right) experiment results for penetration in tissue model with a 1mm bead welded to $\{18, 20, 26\}$ gauge needles (1.27, 0.91, 0.46 mm in diameter).

Several tests including tissue penetration, self-assembly, and MRI tracking were conducted in a Siemen's Skyra 3T clinical MRI scanner. The penetration tests used a brain model composed of a solidified 0.5% agarose gel solution [32]. A 30 mm block of agarose was placed near the isocenter of the scanner. The delivery component, loaded with either an 18, 20, or 26-gauge needle was placed against the block. At least five trials were recorded for each needle size. Experiment results are summarized in Fig. 10. As expected, penetration distance increases as the needle diameter decreases (the gauge increases).

Figure 11 shows photos from two experiments with Gauss gun self-assembly and membrane penetration. Each experiment fired 18-gauge needle tips welded to 1 mm spheres into a membrane model, a water balloon filled with blue dye. The first experiment used a *delivery* and a *trigger* component, while the second experiment added a *barrel* component and demonstrated long-range delivery.

The MRI can acquire pre-operative and post-operative images, as depicted in Fig. 12, showing the membrane model before and after Gauss gun deployment, assembly, and firing. Figs. 12a and 12b also show how individual components of the Gauss gun can be tracked in real-time using fast line scans [4].

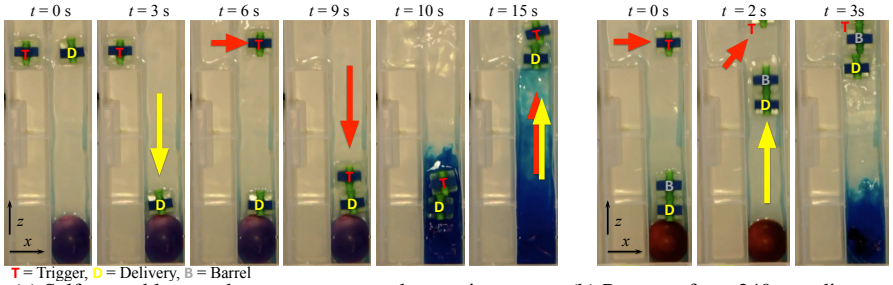

(a) Self-assembly, membrane puncture, and retraction (b) Puncture from 240 mm distance

Fig. 11 Experiment within MRI bore. The membrane model is a water balloon filled with dye.

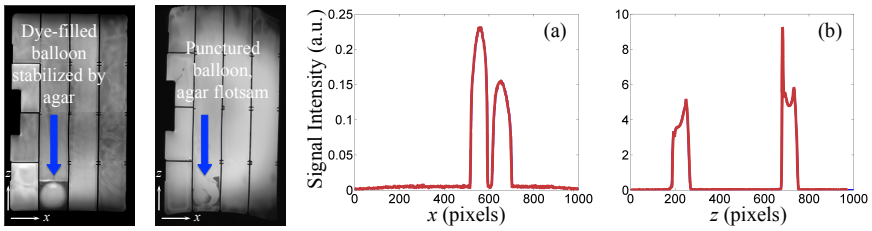

Fig. 12 (left) MRI images showing dye-filled balloon before and after penetration. (right) MRI projections of the Gauss gun components. (a) Projection along the x-axis corresponding to Fig. 11a, frame 2. (b) Projection along the z-axis corresponding to Fig. 11a, frame 3.

6 Future Directions

Current results provide a theoretical and experimental foundation for robot design, tracking, and motion control. Clinically-relevant force magnitudes as well as multi-axis control have been demonstrated. Future efforts should be directed toward both improving the technology and on tailoring it to specific clinical applications.

With regard to technology advances, this includes developing methods to increase actuation forces and imaging rates while still maintaining image fidelity. One approach currently under development is the design of imaging pulse sequences that simultaneously perform propulsion. A second approach is to develop new ways to exploit the large intermagnetic forces between ferrous particles, for example, to perform drug release via robot docking [33]. Such technology improvements may also enable applications involving motion control of micron-scale particles inside the body—something that cannot be achieved with current clinical gradient coils.

References

1. G. Kósa, P. Jakab, G. Székely, and N. Hata, "MRI driven magnetic microswimmers," *Biomedical microdevices*, vol. 14, no. 1, pp. 165–178, 2012.

2. A. Chanu, O. Felfoul, G. Beaudoin, and S. Martel, "Adapting the clinical MRI software environment for real-time navigation of an endovascular untethered ferromagnetic bead for future endovascular interventions," *Magnetic Resonance in medicine*, vol. 59, no. 6, pp. 1287–1297, Jun. 2008.
3. J.-B. Mathieu, G. Beaudoin, and S. Martel, "Method of propulsion of a ferromagnetic core in the cardiovascular system through magnetic gradients generated by an MRI system," *Biomedical Engineering, IEEE Transactions on*, vol. 53, no. 2, pp. 292–299, 2006.
4. O. Felfoul, J.-B. Mathieu, G. Beaudoin, and S. Martel, "In vivo MR-tracking based on magnetic signature selective excitation," *Medical Imaging, IEEE Transactions on*, vol. 27, no. 1, pp. 28–35, 2008.
5. M. Ho, A. B. McMillan, J. M. Simard, R. Gullapalli, and J. P. Desai, "Towards a meso-scale SMA-actuated MRI-compatible neurosurgical robot," *IEEE Transaction on Robotics*, vol. 28, no. 1, pp. 213–222, 2012.
6. G. S. Fischer, A. Krieger, I. Iordachita, C. Csoma, L. L. Whitcomb, and G. Fichtinger, "MRI compatibility of robot actuation techniques–a comparative study," in *Medical Image Computing and Computer-Assisted Intervention–MICCAI 2008*. Springer, 2008, pp. 509–517.
7. S. Martel, J.-B. Mathieu, O. Felfoul, A. Chanu, E. Aboussouan, S. Tamaz, P. Pouponneau, L. Yahia, G. Beaudoin, G. Soulez, and M. Mankiewicz, "Automatic navigation of an untethered device in the artery of a living animal using a conventional clinical magnetic resonance imaging system," *Applied Physics Letters*, vol. 90, no. 11, pp. 114 105–114 105–3, Mar 2007.
8. P. Vartholomeos, L. Qin, and P. E. Dupont, "MRI-powered actuators for robotic interventions," in *IEEE Int. Rob. and Sys.*, 2011, pp. 4508–4515.
9. P. Vartholomeos, C. Bergeles, L. Qin, and P. E. Dupont, "An MRI-powered and controlled actuator technology for tetherless robotic interventions," *Int. J. Rob. Res.*, vol. 32, no. 13, pp. 1536–1552, 2013.
10. D. Y. Song, E. C. Burdette, J. Fiene, E. Armour, G. Kronreif, A. Deguet, Z. Zhang, I. Iordachita, G. Fichtinger, and P. Kazanzides, "Robotic needle guide for prostate brachytherapy: clinical testing of feasibility and performance," *Brachytherapy*, vol. 10, no. 1, pp. 57–63, 2011.
11. H. Su, D. C. Cardona, W. Shang, A. Camilo, G. Cole, D. C. Rucker, R. J. Webster, G. S. Fischer *et al.*, "A MRI-guided concentric tube continuum robot with piezoelectric actuation: a feasibility study," in *Robotics and Automation (ICRA), 2012 IEEE International Conference on*. IEEE, 2012, pp. 1939–1945.
12. N. V. Navkar, Z. Deng, D. J. Shah, K. E. Bekris, and N. V. Tsekos, "Visual and force-feedback guidance for robot-assisted interventions in the beating heart with real-time MRI," in *Robotics and Automation (ICRA), 2012 IEEE International Conference on*. IEEE, 2012, pp. 689–694.
13. M. G. Schouten, J. G. Bomers, D. Yakar, H. Huisman, E. Rothgang, D. Bosboom, T. W. Scheenen, S. Misra, and J. J. Fütterer, "Evaluation of a robotic technique for transrectal MRI-guided prostate biopsies," *European radiology*, vol. 22, no. 2, pp. 476–483, 2012.
14. D. Beyersdorff, A. Winkel, B. Hamm, S. Lenk, S. A. Loening, and M. Taupitz, "MR imaging–guided prostate biopsy with a closed MR unit at 1.5 T: Initial results," *Radiology*, vol. 234, no. 2, pp. 576–581, 2005.
15. D. Stoianovici, C. Kim, G. Srimathveeravalli, P. Sebrecht, D. Petrisor, J. Coleman, S. B. Solomon, and H. Hricak, "MRI-safe robot for endorectal prostate biopsy," *Mechatronics, IEEE/ASME Transactions on*, vol. 19, no. 4, pp. 1289–1299, 2014.
16. C. Yiallouras, N. Mylonas, and C. Damianou, "MRI-compatible positioning device for guiding a focused ultrasound system for transrectal treatment of prostate cancer," *International journal of computer assisted radiology and surgery*, vol. 9, no. 4, pp. 745–753, 2014.
17. A. T. Becker and R. Kaldawy, "Mri needle biopsy robot, http://www.thingiverse.com/thing:449515," Sep. 2014.
18. O. Felfoul, A. Becker, C. Bergeles, and P. Dupont, "Achieving commutation control of an MRI-powered robot actuator," *Robotics, IEEE Transactions on*, vol. 31, no. 2, pp. 387–399, April 2015.
19. K. Ishiyama, M. Sendoh, A. Yamazaki, and K. Arai, "Swimming micro-machine driven by magnetic torque," *Sensors and Actuators A: Physical*, vol. 91, no. 1, pp. 141–144, 2001.

20. R. C. Ritter, M. S. Grady, M. A. H. III, and G. T. Gillies, *Computer-integrated Surgery: Technology and Clinical Applications*. The MIT Press, 1996, ch. 26 Magnetic Stereotaxis: Computer-Assited, Image-Guided Remote Movement of Implants in the Brain, pp. 363–370.
21. C. J. Walsh, "Image-guided robots for dot-matrix tumor ablation," Ph.D. dissertation, Massachusetts Institute of Technology, Massachusetts Institute of Technology. Dept. of Mechanical Engineering., 2010. [Online]. Available: http://hdl.handle.net/1721.1/61613
22. R. Schill, "General relation for the vector magnetic field of a circular current loop: a closer look," *Magnetics, IEEE Transactions on*, vol. 39, no. 2, pp. 961–967, Mar 2003.
23. C. H. Cunningham, T. Arai, P. C. Yang, M. V. McConnell, J. M. Pauly, and S. M. Conolly, "Positive contrast magnetic resonance imaging of cells labeled with magnetic nanoparticles," *Magnetic Resonance in Medicine*, vol. 53, no. 5, pp. 999–1005, 2005.
24. C. Bergeles, P. Vartholomeos, L. Qin, and P. E. Dupont, "Closed-loop commutation control of an MRI-powered robot actuator," in *IEEE International Conference on Robotics and Automation*, May 2013, pp. 690–695.
25. P. Vartholomeos, M. Akhavan-Sharif, and P. E. Dupont, "Motion planning for multiple millimeter-scale magnetic capsules in a fluid environment," in *IEEE Int. Conf. Rob. Aut.*, May 2012, pp. 1927–1932.
26. A. Eqtami, O. Felfoul, and P. E. Dupont, "MRI-powered closed-loop control for multiple magnetic capsules," in *IEEE/RSJ Int. Conf. Intelligent Robots and Systems*, 2014, pp. 3536–354.
27. A. Becker, Y. Ou, P. Kim, M. Kim, and A. Julius, "Feedback control of many magnetized tetrahymena pyriformis cells by exploiting phase inhomogeneity," in *IEEE/RSJ International Conference on Intelligent Robots and Systems (IROS)*, Tokyo, Japan, Nov. 2013, pp. 3317–3323.
28. A. Becker. (2014, Jan.) "Control n MRI-powered actuators." MATLAB Central File Exchange. [Online]. Available: http://www.mathworks.com/matlabcentral/fileexchange/45331
29. Z. Artstein, "Stabilization with relaxed controls," *Nonlinear Analysis*, vol. 15, no. 11, pp. 1163–1170, 1983.
30. M. Mahvash and P. Dupont, "Mechanics of dynamic needle insertion into a biological material," *Biomedical Engineering, IEEE Transactions on*, vol. 57, no. 4, pp. 934–943, April 2010.
31. A. T. Becker, O. Felfoul, and P. E. Dupont, "Toward tissue penetration by MRI-powered millirobots using a self-assembled Gauss gun," in *IEEE International Conference on Robotics and Automation (ICRA)*, Seattle, WA, USA, May 26-30 2015.
32. I. Howard, M.A, B. Abkes, M. Ollendieck, M. Noh, R. C. Ritter, and G. Gillies, "Measurement of the force required to move a neurosurgical probe through in vivo human brain tissue," *Biomedical Engineering, IEEE Transactions on*, vol. 46, no. 7, pp. 891–894, July 1999.
33. V. Iacovacci, G. Lucarini, L. Ricotti, P. Dario, P. E. Dupont, and A. Menciassi, "Untethered magnetic millirobot for targeted drug delivery," *Biomedical microdevices*, vol. 17, no. 3, pp. 1–12, 2015.